JOURNAL OF GEOPHYSICAL RESEARCH: SOLID EARTH, VOL. 118, 1–12, doi:10.1002/jgrb.50090, 2013

Elastic laboratory measurements and modeling of saturated basalts

Ludmila Adam,[1,2] and Thomas Otheim[1]

Received 6 August 2012; revised 7 January 2013; accepted 10 January 2013.

[1] Understanding the elastic behavior of basalt is important to seismically monitor volcanoes, subsea basalts, and carbon sequestration in basalt. We estimate the elastic properties of basalt samples from the Snake River Plain, Idaho, at ultrasonic (0.8 MHz) and seismic (2–300 Hz) frequencies. To test the sensitivity of seismic waves to the fluid content in the pore structure, measurements are performed at three saturation conditions: saturated with liquid CO_2, water, and dry. When CO_2 replaces water, the P-wave velocity drops, on average, by 10%. Vesicles and cracks, observed in the rock microstructure, control the relaxation of pore-fluid pressures in the rock as a wave propagates. The bulk and shear moduli of basalts saturated with liquid CO_2 are not frequency dependent, suggesting that fluid pore pressures are in equilibrium between 2 Hz and 0.8 MHz. However, when samples are water saturated, the bulk modulus of the rock is frequency dependent. Modeling with Gassmann's equations predicts the measured saturated rock bulk modulus for all fluids for frequencies below 20 Hz but underpredicts the water-saturated basalt bulk modulus for frequencies greater than 20 Hz. The most likely reason is that the pore-fluid pressures are unrelaxed. Instead, the ultrasonic frequency rock moduli are modeled with high-frequency elastic theories of squirt flow and Kuster–Toksöz (KT). Although KT's model is based on idealized pore shapes, a combination of spheres (vesicles) and penny-shaped cracks (fractures) interpreted and quantified from petrographical data predicts the ultrasonic dry and saturated rock moduli for the measured basalts.

Citation: Adam, L., and T. Otheim (2013), Elastic laboratory measurements and modeling of saturated basalts, *J. Geophys. Res. Solid Earth*, *118*, doi:10.1002/jgrb.50090.

1. Introduction

[2] Most studies for geologic CO_2 sequestration have focused on sedimentary rocks and laboratory and numerical experiments aim to monitor the movement of this fluid in sandstone and carbonate rocks [*Wang et al.*, 1998; *Wang and Nur*, 1989; *Grombacher et al.*, 2012; *Xue and Ohsumi*, 2004]. However, more recent research suggests basalt flows as potential reservoirs for CO_2 sequestration [*Bachu et al.*, 1994; *McGrail et al.*, 2011; *Gislason et al.*, 2010]. Although basalts are not commonly thought of as fluid reservoirs, significant capacity exists in the top- and bottom-flow layers as well as in the cracks and fractures of the inner flows. Basalts may be attractive targets for possible CO_2 sequestration reservoirs, being widespread throughout the world and composed of minerals that can trap CO_2 by precipitation to carbonates [*Bachu et al.*, 1994; *Oelkers et al.*, 2008; *McGrail et al.*, 2006; *Otheim et al.*, 2011]. Mineral trapping in basalts has been observed to occur over a period of 30–60 weeks in the laboratory [*Schaef et al.*, 2010; *Otheim et al.*, 2011], but the initial changes in the reservoir happen when CO_2 mixes or fully substitutes reservoir water. Seismic methods may be used to monitor the movement of the CO_2 plume at this fluid substitution state as well as in the mineralization process. Laboratory measurements on rock samples help establish the feasibility of monitoring fluid movement by quantifying the changes in elastic rock properties. Monitoring fluid substitution in basalts with seismic waves can be extended to volcanoes and subsea oceanic crust, where CO_2 and water coexist and lead to hydrothermal alteration [*Goldberg*, 2011; *Seront et al.*, 1998; *Lopez and Williams*, 1993; *Lebedev and Kern*, 1999].

[3] Water saturation and confining pressure affect the ultrasonic velocity for granite rocks [*Nur and Simmons*, 1969; *Todd and Simmons*, 1972]. In these studies, P- and S-wave velocities for dry and saturated rocks increase as cracks close with increasing pressure. However, elastic measurements on saturated basalts under pressure, where vesicles and cracks both contribute the rock's porosity, are rare [*Adelinet et al.*, 2010; *Adelinet et al.*, 2011]. *Johnston and Christensen* [1997] measure dry and water-saturated basalt samples collected from several Deep Sea Drilling Project locations and analyze ultrasonic velocity data as a function of low-temperature alteration and rock microcracks. An increasing contribution of both of these features in subsea basalts decreases the P- and S-wave velocities. They also observe that stress-relief microcracks are more

[1]Physical Acoustics Laboratory, Department of Geosciences, Boise State University, Boise, Idaho, USA.
[2]IESE and School of Environment, University of Auckland, New Zealand.

Corresponding author: L. Adam, University of Auckland, Science Centre, 23 Symonds Street, Auckland 1142, New Zealand. (l.adam@auckland.ac.nz)

2169-9313/13/10.1002/jgrb.50090

abundant in massive flows than in pillow intervals from these basalts. *Tsuji and Iturrino* [2008] and *Cerney and Carlson* [1999] also measured ultrasonic velocities of saturated basalts and focus on the crack contribution alone on the rock's elasticity.

[4] The compressional wave velocity in rocks increases with water saturation and decreases as cracks open [*Nur and Simmons* 1969; *Batzle et al.*, 1980; *Hadley*, 1976], whereas crack size is known to control the velocity and permeability of basalt samples. *Nara et al.* [2011] observe that the pressure dependency of P- and S-wave velocities is controlled differently depending on crack size and distribution. They compare the effect on velocity from microcracks (created by heating the sample in the laboratory oven) and macrocracks (mechanically generated), showing that microcracks have a greater effect on velocity with pressure than macrocracks. Laboratory measurements in basalts show that the density and orientation of cracks can also be correlated to wave velocities [*Wilkens et al.*, 1991; *Adelinet et al.*, 2010; *Tsuji and Iturrino*, 2008; *Cerney and Carlson*, 1999; *Gueguen and Schubnel*, 2003; *Adelinet et al.*, 2011; *Fortin et al.*, 2011], and vertical seismic profile experiments show significant velocity anisotropy due to in situ aligned fractures in schist [*Schijns et al.*, 2012]. However, the effect of water and liquid CO_2 fluids on wave velocity and the applicability of different fluid substitution models on basalts have not been analyzed.

[5] Most of the aforementioned studies on basalt have modeled laboratory velocities in basalt rocks with ellipsoidal cracks (e.g., disks and penny-shaped cracks), but the combination of vesicle (spherical pores) and crack (compliant pores) porosity is common in top-flow basalts. In these flows, vesicles mostly result from magma degassing and cracks from the cooling process of different mineral crystals. Seismic waves are most sensitive to compressible pores. The compressibility of spherical pores, being equidimensional, makes these significantly less sensitive to changes in the pore fluid than cracks [*Wilkens et al.*, 1991; *Kumar and Han*, 2005]. Not only does the rock pore structure contribute to the elastic response of saturated rocks, but also the CO_2 phase is also an important factor to understand. *Yam and Schmitt* [2011] show that the ultrasonic P- and S-wave velocity drops by 4–5% as CO_2 changes phase from gas to liquid or supercritical state in a ceramic rod. The phase of the saturating fluid is important to characterize because pore pressure relaxation depends on the fluid properties.

[6] Wave propagation disturbs fluid pore pressures in the rock, which can result in the frequency dependence of the rock's elastic moduli. The low-frequency limit of the saturated rock bulk modulus, without assumptions on the pore shape and structure of the rock, can be predicted with Gassmann's relation [*Gassmann*, 1951]. The high-frequency limit of the rock's elastic moduli is often described with models such as the *Mavko and Jizba* [1991] local squirt flow (SF) approximation or *Kuster and Toksöz* [1974]. These models are mainly different in that local SF predicts the rock elasticity for connected pores and cracks but without deterministically describing pore shapes. On the contrary, Kuster–Toksöz (KT) assumes geometrically defined and isolated pores. Although other high-frequency inclusion effective media theories exist, we model some of the more commonly used theories for fluid substitution. The KT's model is attractive to implement on our basalts, because the effective ultrasonic elastic rock moduli can be estimated by combining vesicles (spheres) and cracks (penny shapes) [*Berryman*, 1995]. KT is used in many instances to predict the effects of fluid changes on the rock's elasticity and to invert for the crack aspect ratio distribution in rocks, from laboratory measurements to sonic logs [*Cheng and Toksöz*, 1979; *Smith et al.*, 2009]. Here, we integrate petrographical data to forward model the rock elasticity using KT equations and compare the models with our ultrasonic measurements.

[7] In this study, we analyze the feasibility of elastic wave monitoring of CO_2 substituting water in basalts. This is done by measuring the elastic properties at ultrasonic (MHz) and seismic (2–300 Hz) frequencies for two saturated basalt samples by varying pressure. We mostly focus on the ultrasonic measurements and refer the reader to *Otheim* [2012] for details on the measurements at seismic frequencies. The measured basalt elastic properties for different pore fluids are compared with estimates computed from three rock physics models for fluid substitution: Gassmann, KT, and the Mavko–Jizba approximation to local SF. Gaining an understanding of how fluids and rock petrographical properties affect the elastic behavior helps determine the possibility of seismically monitoring water and CO_2 movement in different basalts.

2. Sample Characterization

[8] The basalt samples in this study were collected near Hagerman, Idaho, in the western Snake River Plain. The Twin Falls regional eruptive center resulted from several volcano eruptions during the late Miocene to Pliocene. Basalt deposits in this region depend on the availability of water and can range from effusive to explosive. Basalts in the Twin Falls region are divided into a number of informal groups and map units as described by *Bonnichsen and Godchaux* [2002]. Based on the locations and bulk rock chemical analyses of these samples, the basalts in this study belong to the Gooding Butte Formation. The age of these basalts corresponds between the Pliocene and Pleistocene, and the flows are interpreted to have been produced by a shield-type volcano.

[9] The physical properties and microstructure of rocks are important to understand the elastic response of basalt as a function of pressure and fluid properties. Such rock petrography analysis also provides the input parameters for modeling elastic theories. Basalt microstructure, mineralogy, porosity, and permeability are characterized using X-ray diffraction (XRD), X-ray fluorescence (XRF), mercury injection porosimetry, helium pycnometry and permeability, computed tomography (CT) scan images, and thin sections.

[10] Figure 1 are thin sections of the basalt samples, where blue represents epoxy filling the pore space, the elongated rectangular minerals are plagioclase, and the olivine and pyroxene crystals have a tan-brownish color. The ground mass in sample B1 is composed of volcanic glass with small crystals of pyroxene and olivine, whereas B2 has no glass, but samples B1 and B2 have phenocrysts of similar size. The maximum vesicle size is greater for sample B1 than

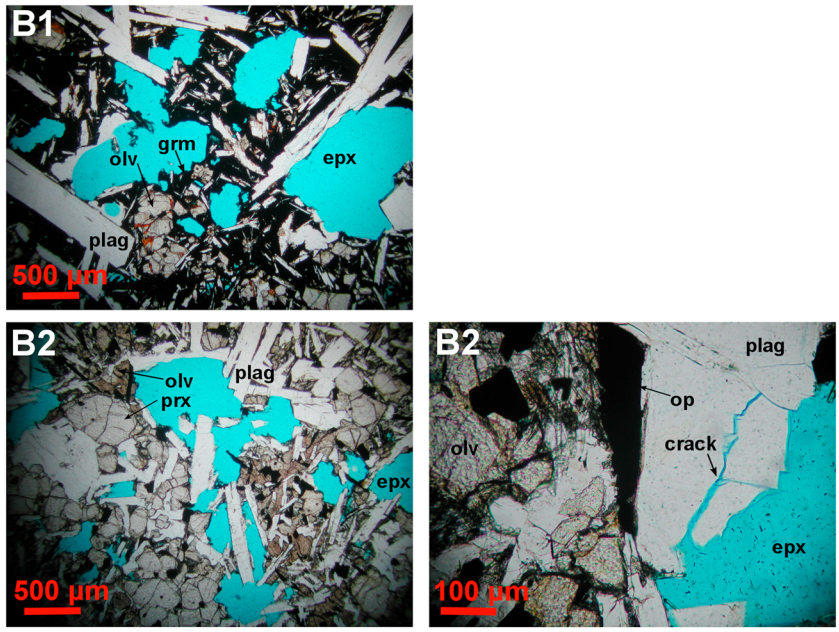

Figure 1. Basalt thin section with blue epoxy (epx) filling the pore space. Crystals of plagioclase (plag), olivine (olv), and pyroxene (prx) can be seen in these sections. The black in sample B1 is groundmass grm—glass and other crystals— whereas the black in B2 are opaque minerals (op). Cracks and compliant pores are observed in both samples, as illustrated by magnification of sample B2.

for sample B2. The large phenocrysts in sample B1 nucleated before ascending to the surface. The combination of glass abundance and phenocrysts nucleation suggests that sample B2 cooled at a slower rate than B1 [*Cashman*, 1993]. Microcracks are widespread in the thin sections, probably resulting from lava cooling. An example of such a crack is highlighted with an arrow in Figure 1. However, compliant pores, as observed at greater magnification in the thin sections, could also be described as "cracks" with greater aperture. Both compliant pores and microcracks significantly contribute to the pressure and fluid saturation velocity sensitivity for these basalt rocks.

[11] To obtain volumetric information on pore space, CT scans, porosity, and permeability measurements are performed. The two basalt rocks are cored to cylinders of 3.8 cm in diameter and are 6.6 cm (B1) and 6 cm (B2) in length. Samples B1 and B2 are visually different, but an XRF analysis shows that the rocks are almost identical in chemical composition and classified as ferrobasalts, having iron oxide (Fe_2O_3) contents greater than 16%. Mineral point counts from the thin sections show 50.4% glass-dominated groundmass in sample B1 but no glass in B2. Because volcanic glass does not diffract X-rays, it is invisible to XRD analysis. The volumetric mineral composition of the rocks is determined by combining XRD and point-count thin-section data for sample B1. The final estimates on volumetric mineral composition for the samples are summarized in Table 1.

Table 1. Volumetric Mineralogical Composition of the Basalts Based on XRD Measurements[a]

Minerals (%)	Glass	Plagioclase	Pyroxene	Olivine	Gypsum	Ilmenite
B1	50.4	31.2	0.0	16.4	0.8	1.2
B2	0.0	67.3	15.1	12.2	0.7	4.7

[a]XRD data for sample B1 are weighted by the volume of glass estimated from a thin-section point count.

[12] CT scanning is a nondestructive method to image the internal structure of rocks. Slices of the CT volume for the basalt samples are shown in Figure 2, where the grayscale is proportional to density: black is pore space and white represents high density. For these rocks, the lightest shades in the CT scan images correspond to olivine and pyroxene minerals, whereas plagioclase is easily identified as midgray longitudinal crystals. Sequential slices and 3-D renderings provide information about the volumetric shape and size of voids, with pores shapes being either almost perfect spheres (vesicle) or compliant pores and cracks. The pixel resolution of these images is 40 µm; thus, vesicles and cracks smaller than this cannot be imaged with this technique.

[13] Finally, rock porosity is estimated with two methods: helium pycnometry and mercury injection porosimetry. Helium porosity and permeability are measured with a

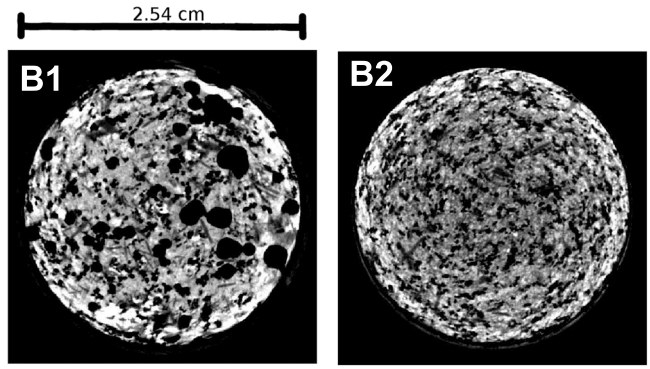

Figure 2. CT scan images of sample B1 and B2, mineral density increases from dark to light gray, and black is pore space.

CMS300 instrument (from CoreLabs). Under variable confining pressure, pore volume is estimated using an advanced Boyle's law, whereas permeability is estimated with an integrated form of the combined Darcy, Klinkenberg, and Forchheimer equations. Quality control is ensured with a standard sample that is run with every measurement. Data summarizing the helium porosity and permeability with variable confining pressure are listed in Table 2. Sample B1 shows greater pressure sensitivity for permeability and porosity than sample B2. For these samples, porosity is largely dominated by vesicles, but permeability data suggest that microcracks or smaller pores connect these vesicles.

[14] Mercury porosity is estimated from measurements performed with a mercury capillary pressure system with a maximum injection pressure of 414 MPa [*Sondergeld et al.*, 2010]. Porosities measured with helium and mercury are 19.16% and 9.88% for sample B1 and 13.88% and 10.27% for sample B2, respectively. Because helium has a lower viscosity than mercury, smaller pores and cracks can be reached with helium gas; thus, the porosity estimated with helium is greater than with mercury. It is important to note that the helium and mercury porosity are measured on different samples and rock volumes (mercury rock volume = 15 cm^3 compared with helium rock volume = 220 cm^3); thus, some of the porosity difference could be due to sample volume and heterogeneity. Figure 3 is a graph of pore throat size and volume of mercury injected, showing that, for sample B2, 80% of the porosity results from large pores (10–100 μm) and 20% of the total porosity can be interpreted as cracks or compliant pores smaller than 1 μm. Sample B1 has a similar bimodal distribution between large vesicles and cracks but with some porosity corresponding to pore sizes between 1 and 10 μm. We also estimate total porosity using the 3-D CT scan images resulting in a porosity of 19.06% and 13.18% for samples B1 and B2, respectively. When compared with the 6.9 MPa measured helium porosity (Table 2), these numbers are within 3% of each other.

[15] Helium porosity measures connected porosity for a gas. The fact that the CT scan and helium estimated porosities agree means that the total porosity is about the same as the effective (connected) porosity for a gas. However, it is possible that water, having a greater viscosity than helium or CO_2, might not reach all the pores and cracks that helium fills. From the agreement between CT scan porosity and helium pycnometry and visual inspection of CT images and thin sections, helium porosity is used to estimate the density of the rocks and used as an input parameter for the models described in this article. The information we extract from the mercury injection porosimetry is the crack-to-vesicle ratio. For modeling inclusions with KT, we estimate the crack-to-vesicle ratio from mercury injection porosimetry and apply it to the total porosity measured with helium pycnometry. For our samples, although there might be throat pores larger than the upper end of the resolution for mercury injection porosimetry (100 μm), we assume that the crack-to-vesicle ratio for a small rock volume can be upscaled to a larger core sample. Because elastic properties of fluid-saturated rocks are most sensitive to cracks and compliant pores, characterizing the physical properties of rocks is vital to understand elastic wave propagation in basalts.

Table 2. Helium Permeability[a] (k) and Porosity (φ) as a Function of Confining Pressure

Pressure/Sample	k_{B1} (mD)	k_{B2} (mD)	φ_{B1} (%)	φ_{B2} (%)
6.9 MPa	1.63	0.19	19.16	13.88
12.4 MPa	1.31	0.16	18.68	13.62
17.2 MPa	1.12	0.16	18.41	13.52
Change 7–17 MPa (%)	32	18	4	3

[a]Permeability is corrected for gas slippage.

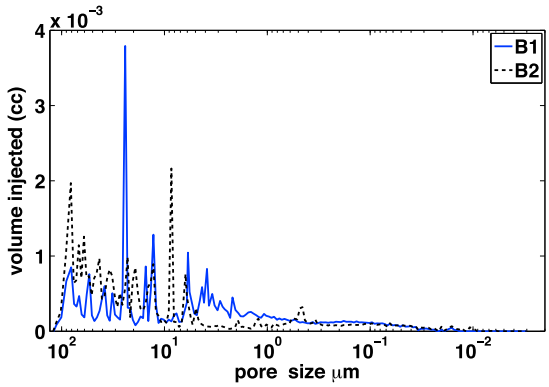

Figure 3. Pore throat size distribution from mercury porosimetry. Vesicles correspond to pore throat sizes 10–100 μm, whereas cracks and compliant pores have pore sizes of <1 μm.

3. Data Acquisition

[16] The basalt elastic moduli and wave speeds are measured in an apparatus that combines measurements at seismic (2–300 Hz) and ultrasonic (10^6 Hz) frequencies. The setup for the basalt measurements is sketched in Figure 4, but details about the apparatus are described in

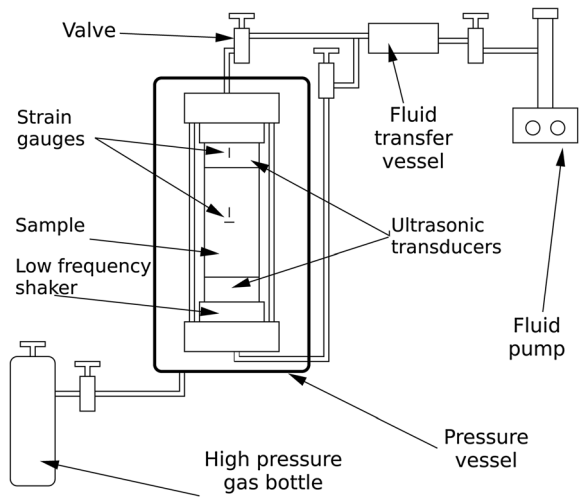

Figure 4. Experimental setup showing how pore and confining pressure in the sample are controlled. Elastic measurements are acquired at seismic frequencies with strain gauges and at ultrasonic frequencies with transducers.

Batzle et al. [2006] and *Adam et al.* [2009]. Measurements are made inside a vessel with confining pressures ranging from 11.7 to 25.5 MPa. The upper limit of the confining pressure is bound by safety concerns about pressurization with nitrogen gas. Ultrasonic data are recorded using high-pressure transducers glued to the ends of the sample. The ultrasonic waveform is recorded and the wave propagation time is estimated from the first arrival. Wave speed is then estimated by diving the sample length by this time.

[17] Rock elasticity at seismic frequencies is estimated from a quasi-static stress-strain experiment. Strain due to an applied sinusoidal stress is measured with semiconductor strain gauges glued to the sample. The rock bulk and shear moduli are estimated from the strain ratios between vertical and horizontal deformations on the rock and on an aluminum standard that result from the low-frequency sinusoidal stress applied with a mechanical shaker [*Batzle et al.*, 2006].

[18] Fluid lines into the vessel and through the transducers provide a fluid flow path to the rock, and fluid type and pore pressure are controlled by a high-pressure fluid pump. There are three saturation scenarios under which we collect data for the basalt samples: dry, fully saturated with distilled water, and fully saturated with liquid CO_2. Sample dry conditions are room conditions on a dry summer day in Colorado. Samples are evacuated for half a day before dry experiments and between fluid saturations experiments. Samples are jacketed and a confining pressure with nitrogen gas is applied. Because there is a vacuum in the pore space, the differential pressure for dry measurements acquisition is equal to the confining pressure.

[19] Geologic sequestration of CO_2 and many volcanic processes occur at depths greater than 1 km. At these depths, CO_2 can be in liquid state depending on the temperature gradient of the area. Our experiments are performed at an ambient temperature of 20°C and a constant pore pressure of 8.3 MPa, meaning that the CO_2 filling the pore space is in liquid state. At 20°C, the crossover point for CO_2 gas to liquid phase is 5.7 MPa, thus by keeping the pressure at 8.3 MPa the CO_2 remains liquid. The pore-fluid lines into the sample are connected to a fluid transfer vessel that has a piston separating CO_2 and distilled water. The pressure on both sides of the transfer vessel is equal and the pressure of the distilled water is maintained by a high-precision fluid pump (Teledyne Isco Syringe Pump 65DM), as shown in Figure 4. Keeping the pore pressure of water and CO_2 at 8.3 MPa throughout the experiments results in measurements performed at differential pressures (i.e., confining minus pore pressure) between 3.4 and 17.2 MPa. For the pore pressures in the experiments at 20°C, the density and bulk modulus of CO_2 is 0.832 g/cm^3 and 0.159 GPa, respectively. These values were estimated with the Thermophysical Properties of Fluid Systems program developed by the National Institute of Standards and Technology (NIST) [*Lemmon et al.*, 2012].

4. Results

[20] Ultrasonic P- and S-wave velocities as a function of pressure and fluid type for samples B1 and B2 are plotted in Figure 5. Error bars are the size of the symbols and represent one standard deviation of the velocity estimate, computed as described in *Adam et al.* [2006]. The dominant frequency estimated by applying a fast Fourier transform to the direct arrivals on the ultrasonic data are 0.6 and 0.8 MHz for P- and S-waves, respectively. Overall, sample B2 has a greater P- and S-wave velocity than sample B1, consistent with the higher porosity for sample B1. The velocities increase with differential pressure in both samples, because cracks and compliant pores close as pressure increases. The velocity for sample B1 is more pressure dependent than for sample B2, which is in agreement with the helium permeability and porosity pressure-dependent data (Table 2). When samples are fully saturated with liquid CO_2, there is no significant change in velocity compared with the dry case. However, both samples have, on average, a 10% higher water-saturated velocity than when CO_2 saturated or dry.

[21] The rock physics models considered in this study predict the isotropic effective elastic moduli for saturated rocks. We therefore need to estimate the bulk (K) and shear modulus (μ) of the basalts for different saturation fluids. These moduli are estimated from the P-wave (V_P) and S-wave (V_S) velocities and the rock bulk density (ρ):

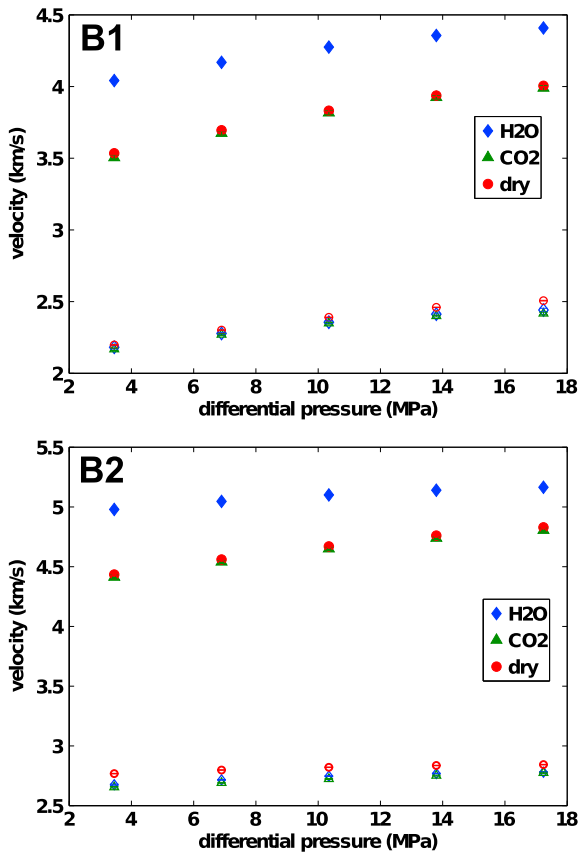

Figure 5. Estimated elastic wave velocity for sample B1 (top) and B2 (bottom) fully saturated with liquid CO_2, water, and dry. Open symbols are S-waves and solid symbols are P-waves. The dominant frequencies are 0.8 and 0.6 MHz for P- and S-waves, respectively. Error bars are the size of the symbols and represent one standard deviation of the velocity estimate.

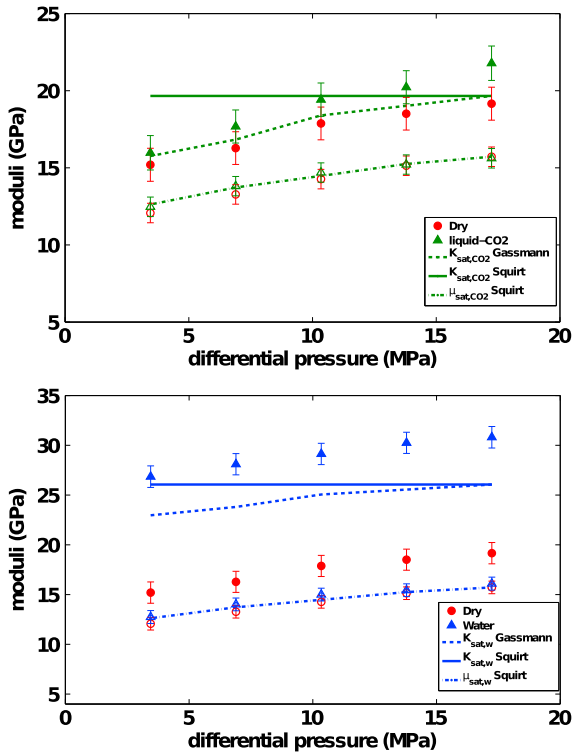

Figure 6. Measured ultrasonic bulk (solid symbols) and shear (open symbols) moduli for sample B1. The moduli for the CO_2-saturated sample (top) and water-saturated sample (bottom) are compared with the measurements on the dry sample. Error bars are one standard deviation of the moduli estimates. The saturated rock moduli modeled by Mavko–Jizba SF and Gassmann are plotted as lines.

$$K = V_P^2\rho - \frac{4}{3}\mu \quad \text{and} \quad \mu = V_S^2\rho. \tag{1}$$

[22] The ultrasonic bulk moduli are plotted as solid symbols in Figures 6 and 7. The estimated bulk modulus of the rock saturated with liquid CO_2 is close to the measurements at dry conditions, resulting from the high compressibility of CO_2. However, the bulk modulus of the basalts increases, on average, by 75% from CO_2 saturated to fully water saturated. The shear modulus (open symbols in Figures 6 and 7) is independent of fluid saturation because the shear modulus of a fluid is zero. Next, we compare estimates of the bulk and shear modulus at ultrasonic and seismic frequencies (2–300 Hz).

[23] Figure 8 shows the saturated rock moduli for sample B2 at the highest differential pressure of 17.2 MPa. The shear modulus is nearly constant with frequency for both water and CO_2 saturation. Although the rock bulk modulus is constant for CO_2 saturation, it is frequency dependent when the sample is fully water saturated. The same behavior is observed for sample B1. In the next section, we test three elastic rock models: Gassmann, the Mavko–Jizba approximation for SF, and KT. Their prediction of the rock effective elasticity is compared with the laboratory measured elastic moduli and velocities in basalts.

5. Elastic Rock Models

[24] In the previous section, we confirmed that velocity and elastic moduli increase as cracks or compliant pores close and that overall fluids increase the elastic bulk modulus. However, the inclusion of fluids in the pore space might result in frequency-dependent moduli. We therefore apply three models for fluid substitution that typically are used in different frequency domains.

[25] A propagating wave disturbs the pore-fluid pressures in a rock. Fluids in equidimensional pores (e.g., vesicles) are not greatly disturbed due to the symmetry of the pore, but cracks or compliant pores build pore pressure as a result of wave induced stress [*Mavko and Jizba*, 1991; *Walsh*, 1969; *Budiansky and O'Connell*, 1976; *Lu and Jackson*, 2006]. If there is enough time within a wave period for the fluid to equilibrate, the pore pressures are said to be "relaxed". If the period is short (high frequency), the pore-fluid pressures may not have enough time to equilibrate and the rock's elastic parameters are termed "unrelaxed". At this state, the rock is stiffer, with greater elastic moduli compared with the relaxed state. The dependence of elastic properties on frequency is called dispersion, and the frequency range at which moduli dispersion dominates depends on the selected model for a review, see *Müller et al.* [2010] and *Mavko et al.* [2003].

[26] Gassmann's relation [*Gassmann*, 1951] is the most widely used fluid substitution model to predict the bulk

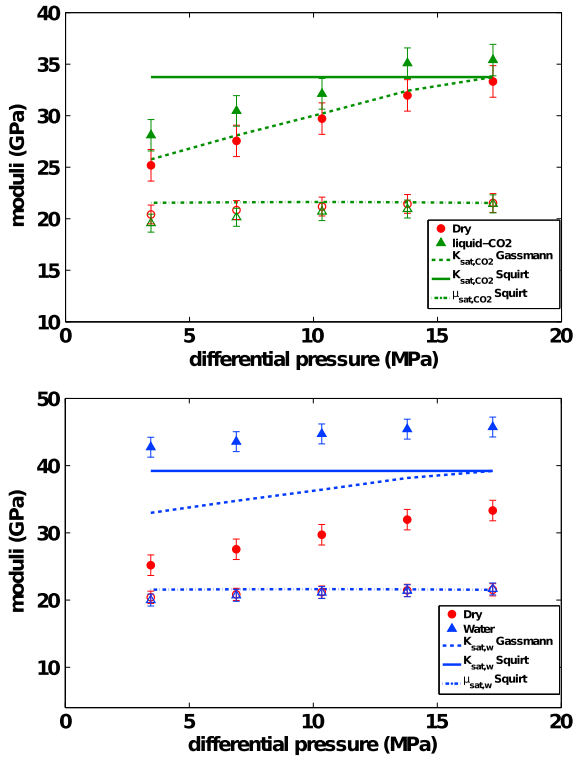

Figure 7. Measured ultrasonic bulk (solid symbols) and shear (open symbols) moduli for sample B2. The moduli for the CO_2-saturated sample (top) and water-saturated samples (bottom) are compared with the dry measurements. Error bars are one standard deviation of the moduli estimates. The saturated rock moduli modeled by Mavko–Jizba SF and Gassmann are plotted as lines.

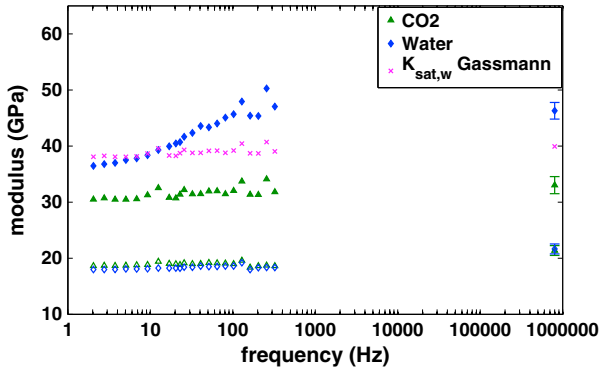

Figure 8. Measured bulk (solid symbols) and shear (open symbols) moduli for sample B2 at 17.2 MPa differential pressure. The shear modulus of the rock and the liquid CO_2-saturated basalt bulk modulus are not frequency dependent, whereas the bulk modulus of the basalt when fully saturated with water is frequency dependent. Measurements are compared with the water-saturated bulk modulus modeled using Gassmann's relation (x symbols).

modulus of saturated rocks. An important assumption in this model is that the fluid pressures in the pores are relaxed, and for many rocks, this means zero or low (seismic) frequencies. Nevertheless, we test the applicability of Gassmann to ultrasonic and seismic frequencies for the measured core samples. We then study two unrelaxed effective elasticity models: SF *Mavko and Jizba* [1991] and *Kuster and Toksöz* [1974]. Both of these models are developed for high frequencies (e.g., ultrasonics). Gassmann's and squirt models are developed to estimate the saturated rock moduli from physical parameters. The KT model is based on inclusions, where pores are deterministically defined with mathematical shapes (e.g., spheres, needles, and penny shapes). Next we briefly introduce the models and compare their predicted moduli with our experimental data on basalts.

5.1. Gassmann's Model

[27] Gassmann's relation is used to predict the bulk modulus of a fully saturated rock (K_{sat}), from the bulk modulus of the dry rock (K_{dry}), the fluid (K_{fl}), the mineral (K_m), and the rock porosity (φ) [*Gassmann*, 1951]:

$$K_{sat} = K_{dry} + \frac{\left(1 - \frac{K_{dry}}{K_m}\right)^2}{\frac{\varphi}{K_{fl}} + \frac{(1-\varphi)}{K_m} - \frac{K_{dry}}{K_0^2}}. \quad (2)$$

[28] Equation (2) is based on the following assumptions: (1) pore pressure is in equilibrium between pores, (2) the porous frame consists of a single solid material (monomineralic rock), (3) pores are in flow communication and are homogeneously fully filled with a nonviscous fluid, (4) the system is closed, and (5) the pore fluid does not chemically influence the solid frame. Because the bulk moduli of the minerals composing the studied basalt rocks are known and not highly variable, the effective mineral bulk modulus can be assumed as monomineralic. For our basalt samples, K_m is estimated using the Voigt-Reuss-Hill average based on the volumetric fraction of minerals from XRD data (Table 1) and tabulated K_m for each mineral [*Mavko et al.*, 2003]. K_m is 80.1 and 84.1 GPa for samples B1 and B2, respectively. The bulk modulus of the saturating fluids is estimated using the NIST Thermophysical Properties of Fluid Systems program [*Lemmon et al.*, 2012]. At the fluid pressure and temperature of these experiments, K_{fl} is 0.159 and 2.237 GPa for CO_2 and water, respectively. We use helium porosity (Table 2) and the measured bulk modulus of the rock dry at seismic and ultrasonic frequencies as input parameters for Gassmann's modeling.

[29] Figures 6 and 7 compare the ultrasonic measured rock bulk modulus with the predicted saturated rock modulus (dashed lines), for both CO_2 and water, estimated with Gassmann's equation (Equation (2)). Gassmann's relation closely predicts the CO_2-saturated rock modulus for both samples but underpredicts the water-saturated rock bulk modulus by up to 40%.

[30] The measured seismic and ultrasonic moduli for sample B2 at the highest differential pressure of 17.2 MPa are plotted in Figure 8. The CO_2-saturated rock bulk modulus does not depend on frequency. However, when the sample is water saturated, the bulk modulus increases with frequency. When we model the water-saturated bulk modulus from the dry measurements at seismic frequencies, we observe that Gassmann's relation predicts the water bulk modulus for frequencies lower than 20 Hz (Figure 8). To quantify the velocity dispersion at ultrasonic frequencies, we use the high-frequency models of Mavko–Jizba SF and KT for saturated rocks.

5.2. Mavko–Jizba SF Model

[31] As a wave propagates through a rock, local flow at grain scales (microflow) between compliant and stiff pores changes pore-fluid stresses. The Mavko–Jizba SF model [*Mavko and Jizba*, 1991] describes the low-frequency (Gassmann–Biot) and high-frequency limits for elastic moduli dispersion. The model is used to predict the saturated moduli of a rock without parameterizing the geometry of the pores. Pore compressibility (a generalization of the pore shape) is included in the general definition of the rock's porosity by separating soft (φ_{soft}) and stiff porosity. Stiff porosity corresponds to pores that deform similarly in all directions, thus not creating fluid flow. φ_{soft} comes from compliant pores, cracks, and grain boundaries, which compress relatively easy with the passage of a wave and are responsible for SF. In basalt rocks, such flow will result from compliant pores or cracks, because grain boundaries are mostly welded. φ_{soft} is highly dependent on pressure (σ); thus, the pressure dependence of the dry rock moduli is one of the main model parameters for SF. The model assumes that the rock's cracks are all closed at the highest hydrostatic confining stress (σ); thus, the contribution from soft porosity to the moduli dispersion is negligible at that pressure, because local flow does not exist. Three other assumptions are included in the derivation: (1) the rocks are fully saturated; (2) the rock is monomineralic, elastic, and isotropic; and (3) the fluid bulk modulus is much smaller than the mineral bulk modulus. The effective high-frequency (ultrasonic) unrelaxed wet frame modulus (K_{uf}) is approximated by [*Mavko and Jizba*, 1991] as

$$\frac{1}{K_{uf}} \approx \frac{1}{K_{dry}}\bigg|_{high\sigma} + \left(\frac{1}{K_{fl}} + \frac{1}{K_m}\right)\varphi_{soft}(\sigma). \quad (3)$$

[32] The second term in Equation (3) adds the crack porosity contribution (soft porosity) to the rock compressibility of

the rock wet frame. However, because this term is small, it is often ignored. We thus estimate K_{uf} only from the first term in Equation (3), which means that K_{uf} is constant with varying differential pressure. The effective high-frequency unrelaxed shear modulus is

$$\frac{1}{\mu_{uf}(\sigma)} = \frac{1}{\mu_{dry}(\sigma)} + \frac{4}{15}\left(\frac{1}{K_{uf}} - \frac{1}{K_{dry}(\sigma)}\right), \tag{4}$$

where the contribution of soft porosity to the unrelaxed effective shear modulus is implicit in the μ_{dry} and K_{dry} dependence on differential pressure (σ). Equations (3) and (4) are not the saturated bulk and shear moduli at high frequencies but correspond to the moduli of the unrelaxed wet frame of the rock. The rock saturated bulk modulus at high frequency can be obtained by replacing K_{dry} with K_{uf} in Equation (2). Again, because K_{uf} is constant with pressure, so would be the saturated bulk modulus estimated with the squirt model (K_{squirt}). The shear modulus does not change with fluids; thus, μ_{squirt} (e.g., μ_{uf}) is constant with fluid substitution but is pressure dependent.

[33] Figures 6 and 7 compare the SF fluid-saturated unrelaxed rock bulk and shear moduli to the experimentally measured modulus for the basalt samples. The high-frequency saturated rock bulk modulus is constant with pressure (K_{squirt}), because we approximate K_{uf} by a single value $K_{dry,high\ \sigma}$. To be able to incorporate the pressure dependence in μ_{squirt}, we analyze velocities. Figure 9 is the measured dry and water-saturated P-wave velocities compared with the predicted velocities by Gassmann and SF. The underprediction of the SF model, compared with the measured saturated bulk modulus, is probably due to open cracks at the highest differential pressure (17.2 MPa). Based on this observation, we assume that cracks are open in our rocks for the measured pressure range 3.4–17.2 MPa. We therefore model the saturated basalt bulk moduli following the KT approach, where geometry and volumetric distribution of pores are explicitly defined.

5.3. KT Model

[34] *Kuster and Toksöz* [1974] model the effective elastic parameters for dry and fluid-saturated rocks based on idealized pore shapes. The equations are developed based on single-scattering theory, where the inclusions are smaller than the wavelength. The model is applicable for inclusions that are randomly distributed, isolated, and in small volumes. Different from SF, there is no fluid flow between the pores or cracks (inclusions). Therefore, this model may be applicable to high-frequency measurements (e.g., ultrasonics). Because of the significant difference in the experimentally measured bulk modulus at low and ultrasonic frequencies (Figure 8), we can assume that the pore pressures are unrelaxed in our samples at this high frequency. The model also assumes dilute concentrations of the inclusions, which together with the matrix form an elastic, isotropic, and linear media.

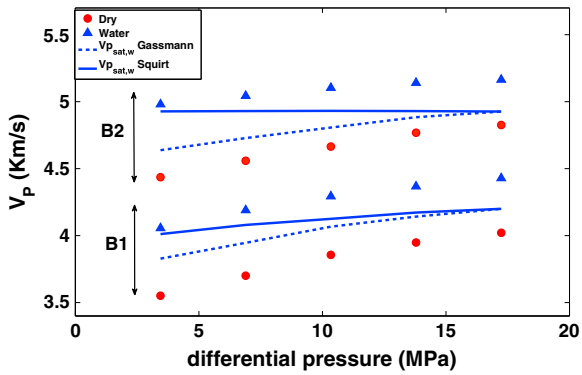

Figure 9. Estimated ultrasonic dry and water-saturated ultrasonic P-wave velocity for samples B1 and B2 (symbols). The wave velocity of water saturated basalt modeled by Mavko–Jizba SF and Gassmann are plotted as lines.

[35] The KT formulation for effective rock moduli can be modeled for one inclusion type or as a sum of volumetric contributions of different inclusion shapes. The various inclusions can be mixed and summed to represent a combination of pore shapes to predict the effective bulk (K_{KT}) and shear (μ_{KT}) moduli [*Kuster and Toksöz*, 1974]:

$$(K_{KT} - K_m)\frac{K_m + \frac{4}{3}\mu_m}{K_{KT} + \mu_m} = \sum_{i=1}^{N} x_i (K_i - K_m) P^{mi} \tag{5}$$

$$(\mu_{KT} - \mu_m)\frac{\mu_m + \zeta_m}{\mu_{KT} + \zeta_m} = \sum_{i=1}^{N} x_i (\mu_i - \mu_m) Q^{mi}, \tag{6}$$

where $\zeta_m = \frac{\mu_m}{6}\left(\frac{9K_m + 8\mu_m}{K_m + 2\mu_m}\right)$.

[36] The bulk and shear moduli of the inclusions are represented by the subscript i in Equations (5) and (6). Because our inclusions are fluid-filled, $K_i = K_{fl}$. The shear modulus of gases or low-viscosity liquids is equal to zero. Therefore, the shear modulus (μ_i) of the inclusion is set to zero for air (dry), liquid CO_2, and water. x_i is the volume fraction of each inclusion type multiplied by the porosity ($\sum_i^N x_i = \varphi$). The coefficients P^{mi} and Q^{mi} give the contribution of the shape of the inclusion to the rock's effective modulus. We model the inclusions in two ways: (1) assuming all the porosity comes from penny-shaped cracks (i.e., disks) and (2) a mixture of spheres and penny-shaped cracks. The equations for the coefficients P and Q for spheres and pennies are [*Kuster and Toksöz*, 1974; *Walsh*, 1969; *Berryman*, 1995]

$$P^{mi}_{spheres} = \frac{K_m + \frac{4}{3}\mu_m}{K_i + \frac{4}{3}\mu_m} \quad Q^{mi}_{spheres} = \frac{\mu_m + \zeta_m}{\mu_i + \zeta_m}$$

$$P^{mi}_{penny} = \frac{K_m + \frac{4}{3}\mu_i}{K_i + \frac{4}{3}\mu_i + \pi\alpha\beta_m}$$

$$Q^{mi}_{penny} = \frac{1}{5}\left(1 + \frac{8\mu_m}{4\mu_i + \pi\alpha(\mu_m + 2\beta_m)} + 2\frac{K_i + \frac{2}{3}(\mu_i + \mu_m)}{K_i + \frac{4}{3}\mu_i + \pi\alpha\beta_m}\right)$$

$$\beta_m = \mu_m \frac{(3K_m + \mu_m)}{3K_m + 4\mu_m}, \tag{7}$$

where α is the aspect ratio of the inclusions. It represents the ratio of the short-to-long axis of an ellipse ($\alpha = a/b$) as sketched in Figure 11. For sample B2, the modeled KT dry and water-saturated rock moduli for penny shapes alone are plotted with the data in Figure 10. Note that although the bulk modulus of the basalt dry and water-saturated can be modeled with an α between 0.11 and 0.17 to fit the experimental data, the shear modulus is fit by an α of half these values. Similar observations apply to sample B1. From the thin sections and CT scans for samples B1 and B2, it is clear

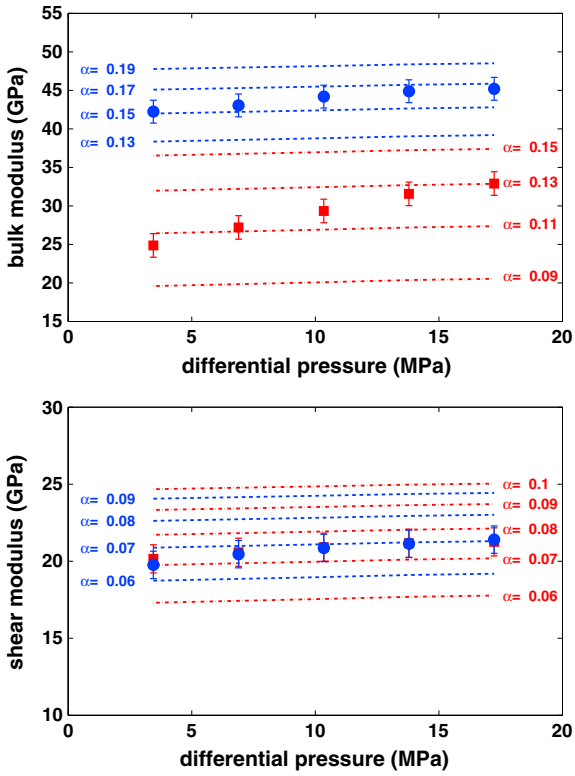

Figure 10. Measured ultrasonic bulk and shear modulus for dry (square symbols) and water-saturated (circle symbols) sample B2. Dotted-dashed and dashed lines are the modeled dry and water-saturated KT moduli, respectively, for a rock with penny-shaped cracks alone. Several crack aspect ratios α are considered.

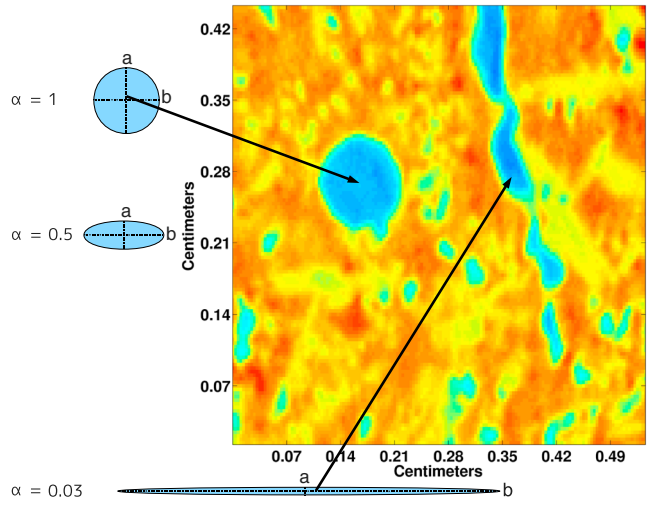

Figure 11. Slices of a CT scan are used to illustrate the inclusion shapes interpreted for the KT model. Blue is porosity, and red and yellow represent higher density minerals, with red being the highest. Cracks and compliant pores are modeled as ellipsoidal penny shapes. The crack aspect ratio is estimated by dividing the ellipse minor axis (a) by the major axis (b). As an example, a low aspect ratio pore is represented by a penny-shaped inclusion with α = 0.03, and other values for α are plotted for reference. Vesicles (the void to the left of the image) are modeled as spheres rather than a circular penny.

that penny-shaped cracks alone do not represent the pore structure of the rock, because spherical vesicles dominate the basalt porosity. On the contrary, if only spheres are modeled as the rock inclusions, the modeled KT water-saturated rock bulk modulus overestimates the measurements by 40%.

[37] We therefore model the contribution of spheres (vesicles) and penny-shaped cracks observed in CT scans in Figures 2 and 11. Also, based on mercury injection porosimetry (Figure 3), thin sections and CT scans, the pore size distribution can be divided into two groups: vesicles and cracks, with the volumetric distribution split at a pore throat size of 1 μm. The volume fraction contribution of each pore geometry is estimated from the porosity measurements, where spheres and cracks contribute 73% and 27% for sample B1 and 83% and 17% for sample B2, respectively. However, we use the helium porosity estimate in this modeling, weighted by this volume of cracks-to-spheres, as explained in Section 2.

[38] Figures 12 and 13 display the predicted KT moduli for a mixture of spheres and penny cracks as a function of α. For both basalts, the estimate of α that simultaneously fits the bulk and shear modulus for dry and saturated conditions is similar. The rock bulk modulus dry and saturated is best fit for an α equal to 0.039 (B1) and 0.023 (B2), and the shear modulus is predicted for an α between 0.025 and 0.033 (B1) and 0.012 and 0.018 (B2). Although the shear modulus is not best matched with these exact values as for the bulk modulus, the difference is small, considering α represents a

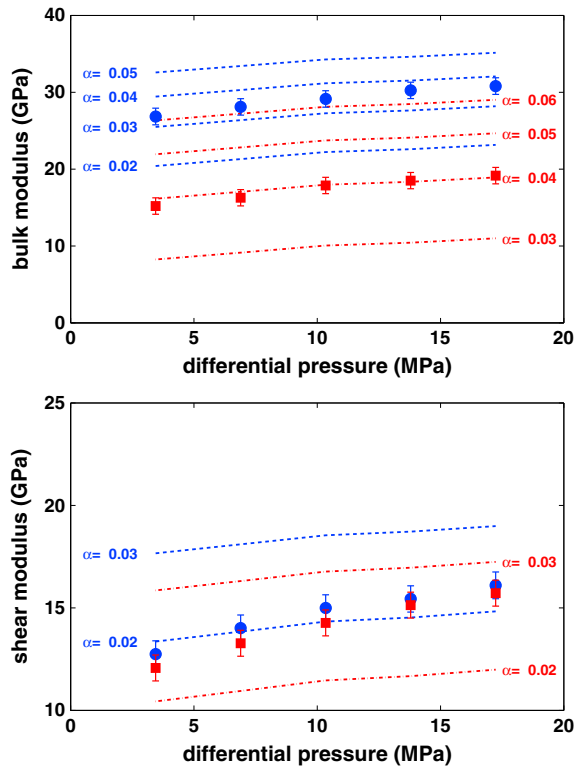

Figure 12. Measured ultrasonic bulk and shear modulus for dry (squared symbols) and water-saturated (circle symbols) sample B1. Dotted-dashed and dashed lines are the modeled dry and water-saturated KT moduli, respectively, for a rock with spheres and penny-shaped cracks. Several values of the crack aspect ratio α are considered.

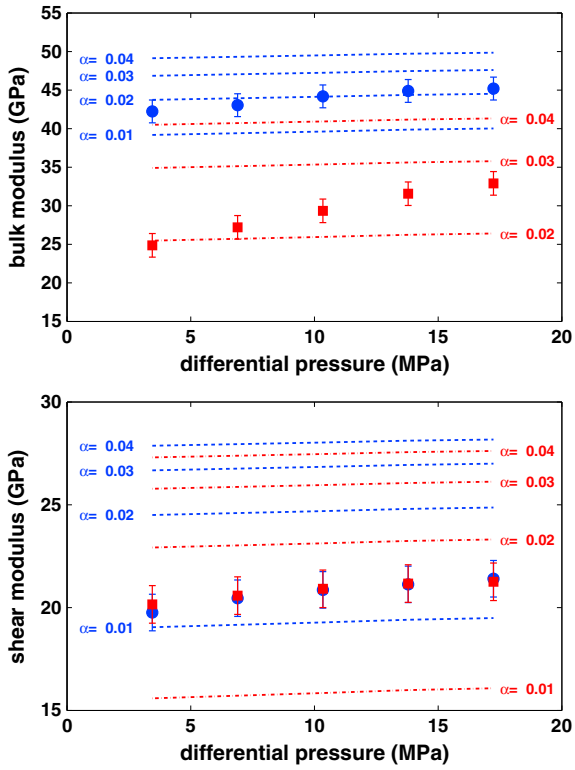

Figure 13. Measured ultrasonic bulk and shear modulus for dry (squared symbols) and water-saturated (circle symbols) sample B2. Dotted-dashed and dashed lines are the modeled dry and water-saturated KT moduli, respectively, for a rock with spheres and penny-shaped cracks. Several values of the crack aspect ratio α are considered.

percent measure of length difference (short vs. long axis) of an ellipse. Thus, a difference in α of 0.005, or a 0.5% in the length of a versus b, is small (Figure 11).

[39] Finally, for a mixture of penny cracks and spheres, we fix α to the best dry estimates (α_{B1} = 0.039 and α_{B2} = 0.023) and vary K_{fl} for the different fluids. Because porosity varies by 4% and 3% with pressure in the samples (Table 2), this information is used to modify the contributions of spheres-to-penny shape ratio of 72–28% at 3.4 MPa and

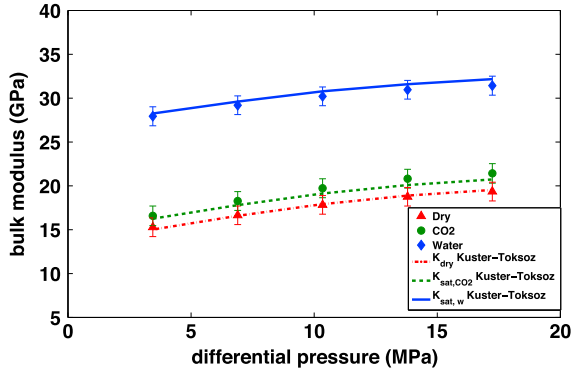

Figure 14. The KT model (lines) with spheres and penny-shaped cracks with an α = 0.04 agrees well with the experimentally estimated ultrasonic bulk modulus (solid symbols) for all pressure and fluids in rock B1.

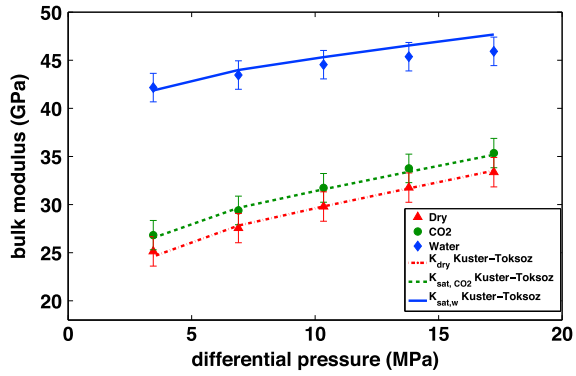

Figure 15. The KT model (lines) with spheres and penny-shaped cracks with an α = 0.02 agrees well with the experimentally estimated ultrasonic bulk modulus (solid symbols) for all pressure and fluids in rock B2.

75–25% at 17.2 MPa for sample B1 and 83–17% at 3.4 MPa and 88–12% at 17.2 MPa for sample B2. Modeling results are shown in Figures 14 and 15 and predict the estimates of the moduli for the three saturation states at ultrasonic frequencies.

6. Discussion

[40] For our samples, Gassmann's model predicts the bulk modulus of CO_2-saturated basalts for all frequencies largely due to the high compressibility of liquid CO_2. When this fluid is added to the dry rock, the bulk stiffness of the basalts increases at most by 5%. The fact that the bulk and shear moduli of our basalts saturated with CO_2 are not frequency dependent suggests that although CO_2 is in liquid state pore pressures are in equilibrium for frequencies between 2 and 10^6 Hz. However, we observe that the bulk modulus of the water-saturated basalts does increase with frequency and the change in *K* from water to CO_2 saturation is, on average, 50%. This results in a change in velocity of 10% when CO_2 substitutes water, which could potentially be monitored in the field with seismic coda waves as modeled by *Khatiwada et al.* [2012]. The frequency dependence of the bulk modulus when basalts are saturated with water can be the result of a difference in fluid viscosity between water and CO_2 (1 and 0.077 cP, respectively). The crossover frequency between where fluid pressures are relaxed or unrelaxed depends on viscosity. However, elasticity models contradict the role of viscosity on the frequency dependence of the rock moduli. For example, viscosity contributes to the denominator in *Budiansky and O'Connell* [1976] but in the numerator in Biot's model [*Biot*, 1956]. This means that the crossover frequency can decrease or increase as the viscosity of the fluid increases. Therefore, although viscosity is probably playing a role in the basalt modulus frequency dependence, modeling its contribution depends on the choice of the elasticity model.

[41] Figure 8 shows the applicability of Gassmann's model for basalt B2. Gassmann's model predicts the water-saturated rock bulk modulus for frequencies below 20 Hz but underpredicts measurements at ultrasonic frequencies for water-saturated basalt (Figures 6 and 7). This is because the modulus is frequency dependent, when the basalts are fully water-saturated. At ultrasonic frequency, the pore-fluid pressures are not in a relaxed state and the rock acts stiffer to

deformation. These results agree with water-saturated basalt measurements by *Adelinet et al.* [2010] performed at low (10^{-2} Hz) and ultrasonic frequency. They observe an increase in the basalt bulk modulus from low to ultrasonic frequencies, interpreted as controlled by the cracks aspect ratio and density. Our crack definition can be from microcracks as those observed in Figure 1 to larger compliant pores that have the same aspect ratio but are larger in size as the one shown in Figure 11. *Adelinet et al.* [2011] proposes a new model to predict the saturated bulk and shear moduli for spherical and spheroidal pore shapes with frequency, but the model is limited to porosities less than 10%. KT model is commonly used to predict laboratory ultrasonic measurements [*Berryman*, 1995; *Tsuji and Iturrino* 2008; *Cerney and Carlson*, 1999]. Because our basalt samples have a porosity greater than 10%, we select KT as the inclusion model to predict the elasticity of our rocks.

[42] At ultrasonic frequencies, SF can dominate and create unrelaxed pore pressures in a rock. The model assumes that at the highest confining pressure all cracks are closed, so the squirt mechanism does not contribute to the high-frequency bulk modulus of the unrelaxed wet frame. At this high pressure, Gassmann's model should predict the experimentally measured bulk modulus of the saturated rock, because local flow would not exist. As pressure decreases, cracks open and SF becomes significant. Thus, for the Mavko–Jizba's SF model to be applicable to laboratory-measured ultrasonic data, the model has to predict the measured bulk modulus at the highest experimental differential pressure. Figures 6 and 7 show that, in our samples, the SF model predicts greater velocities than Gassmann's model but underpredicts the velocity at the highest experimental differential pressure (σ_{high} = 17.2 MPa). This underprediction to the measured data at σ_{high} suggests that cracks and compliant pores are still open at these conditions for our samples. Because cracks are probably dominant at all pressures in our basalts, we estimate the rock's effective elastic parameters by using an inclusion model that can account for them.

[43] Researchers have used KT to model rock properties in basalt. *Tsuji and Iturrino* [2008] studied velocity-porosity relationships in oceanic basalt. They showed that wave velocity is dependent on pressure and porosity and can be described through a spectrum of crack aspect ratios. However, for water-saturated samples, there is no agreement on the value of the estimated α that would satisfy both their P- and S-wave measurements. *Cerney and Carlson* [1999] apply KT to model the P- and S-wave velocities in basalt assuming cracks as the only contributors to porosity. This study fits the wave velocities well by fitting three free parameters: α, K_m, and μ_m. Differently, to model KT, we estimate from XRD and thin-section data the K_m and μ_m for our basalt samples and only fit for α. For the measured basalt samples, KT predicts the measured velocities with pressure for all saturation conditions if we model vesicles—modeled as spheres—together with penny-shaped cracks (Figures 14 and 15). The values of α obtained are qualitatively in agreement with the information in CT scans and thin sections. For the analyzed samples, modeling cracks alone did not simultaneously predict the measured ultrasonic bulk and shear moduli for a common value of α.

[44] Of the three elastic models presented, the KT's model predicts the measured ultrasonic bulk modulus for all pressures and fluids. Although the inclusions are idealized geometric shapes, the pore geometry of basalts might be suited for this effective media model for ultrasonic frequency measurements and can be constrained by incorporating rock petrographical information. However, it is important to keep in mind that the KT equations, with infinite possible combinations of inclusion shapes, could make the presented model parameters one of many possible models that fit the data equally well.

7. Conclusions

[45] Most top-flow sections of basalt formations are dominated by vesicles and cracks formed during degassing and lava cooling. The elastic properties at ultrasonic frequencies of our basalt samples can be modeled with the KT model with a combination of spheres (vesicles) and penny-shaped cracks (fractures). The crack-to-vesicle ratio is estimated by combining petrographical data from helium and mercury porosity, CT scans, XRD, and thin sections. On average, the crack contribution to the total porosity is 20%, whereas the remaining porosity is attributed to spherical vesicles. If cracks (penny shapes) are modeled alone, the experimental ultrasonic bulk and shear moduli for all saturating conditions are not predicted by the KT modeling. The KT model correctly predicts the observed decrease in wave velocity when rock saturation changes from 100% water to 100% liquid CO_2. The observed decrease in velocity due to fluid substitution in the samples measured is, on average, 10%. This change is significant, because it may be large enough to monitor in the field with seismic waves.

[46] Gassmann's model, which assumes relaxed fluid pore pressures, is not applicable to the measured basalts at ultrasonic frequency. At these high frequencies, the water-saturated basalt rock bulk modulus estimated with Gassmann's model underpredicts the experimentally measured data. However, for frequencies lower than 20 Hz, Gassmann's relation does predict the water-saturated rock bulk modulus. This behavior results from the frequency dependence of the water-saturated basalt bulk modulus, with relaxed pore pressures for frequencies below 20 Hz and unrelaxed pressures at ultrasonic frequencies. When samples are CO_2 saturated, Gassmann's model predicts the bulk modulus for all frequencies, because the modulus is not frequency dependent in that case. Based on our samples, basalts fully saturated with liquid CO_2 suggest that pore pressures are in equilibrium for all measured frequencies. This lack of frequency dependence on the rock moduli means that measurements at ultrasonic or logging (~kHz) frequencies could be extrapolated to seismic frequencies for 100% liquid CO_2-saturated basalts. However, more data are required to test the generality of our results.

[47] Although the Mavko–Jizba SF model predicts a higher saturated bulk modulus than Gassmann's model, open cracks at the highest differential pressure of 17.2 MPa mean that the model is not applicable for the data collected here. At pressures higher than we measured, the high-frequency SF mechanism may be applicable.

[48] **Acknowledgments.** We thank Mike Batzle for his invaluable help and the use of the equipment, Manika Prasad for helium pycnometry and permeability measurements and discussions, Craig White for help with the petrography analysis, and Kasper van Wijk for discussions about the results and feedback on the article. George Radziszewski made the CT scan images, Carl Sondergeld made the mercury injection porosimetry, and KT-Geoservices made the XRD analysis. We thank Robert Podgorney, Jerry Fairly, and

Travis McLing for their intellectual involvement and Battelle-DOE (Project # DE-AC07-051D14517) for the financial support for this research. André Revil, Doug Schmitt, and Mathilde Adelinet provided constructive comments that improved this article.

References

Adam, L., M. Batzle, and I. Brevik (2006), Gassmann's fluid substitution and shear modulus variability in carbonates at laboratory seismic and ultrasonic frequencies, *Geophysics*, *71*(6), F173–F183, doi:10.1190/1.2358494.

Adam, L., M. Batzle, K. T. Lewallen, and K. van Wijk (2009), Seismic wave attenuation in carbonates, *J. Geophys. Res.*, *114*(BO6208), doi:10.1029/2008JB005890.

Adelinet, M., J. Fortin, Y. Guéguen, A. Schubnel, and L. Geoffroy (2010), Frequency and fluid effects on elastic properties of basalt: Experimental investigations, *Geophys. Res. Lett.*, *37*(2), L02,303, doi:http://dx.doi.org/10.1029/2009GL041660.

Adelinet, M., J. Fortin, and Y. Gueguen (2011), Dispersion of elastic moduli in a porous-cracked rock: Theoretical predictions for squirt-flow, *Tectonophysics*, *503*(12), 173–181, doi:10.1016/j.tecto.2010.10.012.

Bachu, S., W. Gunter, and E. Perkins (1994), Aquifer disposal of CO_2: Hydrodynamic and mineral trapping, *Energy Conversion and Management*, *35*(4), 269–279, doi:10.1016/0196-8904(94)90060-4.

Batzle, M. L., G. Simmons, and R. W. Siegfried (1980), Microcrack closure in rocks under stress: direct observation, *J. Geophys. Res.*, *85*(B12), 7072–7090.

Batzle, M. L., D.-H. Han, and R. Hofmann (2006), Fluid mobility and frequency-dependent seismic velocity — direct measurements, *Geophysics*, *71*(1), N1–N9, doi:10.1190/1.2159053.

Berryman, J. G. (1995), Rock Physics and Phase Relations, chap. Mixture Theories for Rock Properties, AGU Reference Shelf 3, AGU.

Biot, M. A. (1956), Theory of propagation of elastic waves in a fluid-saturated porous solid. i. low-frequency range, *J. Acoust. Soc. Am.*, *28*(2), 168–178, doi:10.1121/1.1908239.

Bonnichsen, B., and M. M. Godchaux (2002), Late Miocene, Pliocene, and Pleistocene geology of southwestern Idaho with emphasis on basalts in the Bruneau-Jarbidge, Twin Falls, and western Snake River Plain regions, *Tectonic and Magmatic Evolution of the Snake River Plain Volcanic Province: Idaho Geological Survey Bulletin*, *30*, 233–312.

Budiansky, B., and R. O'Connell (1976), Elastic moduli of a cracked solid, *International Journal of Solids and Structures*, *12*(2), 81–97.

Cashman, K. V. (1993), Relationship between plagioclase crystallization and cooling rate in basaltic melts, *Contributions to Mineralogy and Petrology*, *113*(1), 126–142.

Cerney, B., and R. L. Carlson (1999), The effect of cracks on the seismic velocities of basalt from site 990, Southeast Greenland Margin, in *Proceedings of the Ocean Drilling Program, Scientific Results*, vol. 163, edited by H. C. Larsen, R. A. Duncan, J. F. Allan, and K. Brooks, Proceedings of the Ocean Drilling Program, Scientific Results.

Cheng, C. H., and M. N. Toksöz (1979), Inversion of seismic velocities for the pore aspect ratio spectrum of a rock, *J. Geophys. Res.*, *84*, 7533–7544.

Fortin, J., S. Stanchits, S. Vinciguerra, and Y. Guéguen (2011), Influence of thermal and mechanical cracks on permeability and elastic wave velocities in a basalt from Mt. Etna volcano subjected to elevated pressure, *Tectonophysics*, *503*(1), 60–74.

Gassmann, F. (1951), Über die elastizität poröser medien, *Vierteljahrsschrift der Naturforschenden Gesellschaft in Zürich*, *96*, 1–23.

Gislason, S. R., et al. (2010), Mineral sequestration of carbon dioxide in basalt: A pre-injection overview of the carbfix project, *International Journal of Greenhouse Gas Control*, *4*(3), 537–545, doi:DOI: 10.1016/j.ijggc.2009.11.013.

Goldberg, D. (2011), Volcanology: Carbon below the sea floor, *Nature Geosci*, *4*(1), 11–12, doi:10.1038/ngeo1019.

Grombacher, D., T. Vanorio, and Y. Ebert (2012), Time-lapse acoustic, transport, and NMR measurements to characterize microstructural changes of carbonate rocks during injection of CO_2-rich water, *Geophysics*, *77*(3), WA169–WA179, doi:10.1190/geo2011-0281.1.

Gueguen, Y., and A. Schubnel (2003), Elastic wave velocities and permeability of cracked rocks, *Tectonophysics*, *370*(1-4), 163–176, doi:10.1016/S0040-1951(03)00184-7.

Hadley, K. (1976), Comparison of calculated and observed crack densities and seismic velocities in Westerly granite, *J. Geophys. Res.*, *81*(20), 3484–3494.

Johnston, J., and N. Christensen (1997), Seismic properties of layer 2 basalts, *Geophys. J. Int.*, *128*(2), 285–300.

Khatiwada, M., L. Adam, M. Morrison, and K. van Wijk (2012), A feasibility study of time-lapse seismic monitoring of CO_2 sequestration in a layered basalt reservoir, *J. Appl. Geophys.*, *82*, 145–152.

Kumar, M., and D. Han (2005), Pore shape effect on elastic properties of carbonate rocks, in *2005 SEG Annual Meeting*.

Kuster, G. T., and M. N. Toksöz (1974), Velocity and attenuation of seismic waves in two-phase media: Part I. theoretical formulations, *Geophysics*, *39*(5), 587–606, doi:10.1190/1.1440450.

Lebedev, E., and H. Kern (1999), The effect of hydration and dehydration reactions on wave velocities in basalts, *Tectonophysics*, *308*(3), 331–340, doi:10.1016/S0040-1951(99)00106-7.

Lemmon, E., M. McLinden, and D. Friend (retrieved on 2012), NIST Chemistry WebBook, chap. Thermophysical Properties of Fluid Systems, 69, NIST Standard Reference Database, http://webbook.nist.gov.

Lopez, D. L., and S. N. Williams (1993), Catastrophic volcanic collapse: relation to hydrothermal processes, *Science*, *260*, 1794–1796.

Lu, C., and I. Jackson (2006), Low-frequency seismic properties of thermally cracked and argon-saturated granite, *Geophysics*, *71*(6), F147–F159.

Mavko, G., and D. Jizba (1991), Estimating grain-scale fluid effects on velocity dispersion in rocks, *Geophysics*, *56*(12), 1940–1949, doi:10.1190/1.1443005.

Mavko, G., T. Mukerji, and J. Dvorkin (2003), The Rock Physics Handbook: Tools for Seismic Analysis of Porous Media, Stanford-Cambridge Program, Cambridge University Press.

McGrail, B., F. Spane, E. Sullivan, D. Bacon, and G. Hund (2011), The Wallula basalt sequestration pilot project, *Energy Procedia*, *4*(0), 5653–5660, doi:10.1016/j.egypro.2011.02.557.

McGrail, B. P., H. T. Schaef, A. M. Ho, Y.-J. Chien, J. J. Dooley, and C. L. Davidson (2006), Potential for carbon dioxide sequestration in flood basalt, *J. Geophys. Res.*, *111*(B12201), doi:10.1029/2005JB004169.

Müller, T. M., B. Gurevich, and M. Lebedev (2010), Seismic wave attenuation and dispersion resulting from wave-induced flow in porous rocks Ñ A review, *Geophysics*, *75*(5), 75A147–75A164, doi:10.1190/1.3463417.

Nara, Y., P. Meredith, T. Yoneda, and K. Kaneko (2011), Influence of macro-fractures and micro-fractures on permeability and elastic wave velocities in basalt at elevated pressure, *Tectonophysics*, *503*(1), 52–59.

NETL (2010), Carbon sequestration atlas of the United States and Canada, Tech. rep., National Energy Technology Laboratory.

Nur, A., and G. Simmons (1969), The effect of saturation on velocity in low porosity rocks, *Earth and Planetary Science Letters*, *7*(2), 183–193, doi:10.1016/0012-821X(69)90035-1.

Oelkers, E. H., S. R. Gislason, and J. Matter (2008), Mineral carbonation of CO_2, *Elements*, *4*(5), 333–337, doi:10.2113/gselements.4.5.333.

Otheim, T. L. (2012), Monitoring CO_2 sequestration in basalt with elastic waves, Master's thesis, Boise State University.

Otheim, T. L., L. Adam, K. van Wijk, M. L. Batzle, T. McLing, and R. Podgorney (2011), CO_2 sequestration in basalt: Carbonate mineralization and fluid substitution, *The Leading Edge*, *30*(12), 1354–1359, doi:10.1190/1.3672479.

Schaef, H. T., B. P. McGrail, and A. T. Owen (2010), Carbonate mineralization of volcanic province basalts, *International Journal of Greenhouse Gas Control*, *4*(2), 249–261.

Schijns, H., D. Schmitt, P. Heikkinen, and I. Kukkonen (2012), Seismic anisotropy in the crystalline upper crust: observations and modelling from the Outokumpu scientific borehole, Finland, Geophysical Journal International.

Seront, B., T.-F. Wong, J. S. Caine, C. B. Forster, R. L. Bruhn, and J. Fredrich (1998), Laboratory characterization of hydromechanical properties of a seismogenic normal fault system, *Journal of Structural Geology*, *20*(7), 865–881, doi:10.1016/S0191-8141(98)00023-6.

Smith, T. M., C. M. Sayers, and C. H. Sondergeld (2009), Rock properties in low-porosity/low-permeability sandstones, *The Leading Edge*, *28*(1), 48–59, doi:10.1190/1.3064146.

Sondergeld, C., K. Newsham, J. Comisky, M. Rice, and C. Rai (2010), Petrophysical considerations in evaluating and producing shale gas resources, in *SPE Unconventional Gas Conference*.

Todd, T., and G. Simmons (1972), Effect of pore pressure on the velocity of compressional waves in low-porosity rocks, *J. Geophys. Res.*, *77*(20), 3731–3743, doi:doi:10.1029/JB077i020p03731.

Tsuji, T., and G. J. Iturrino (2008), Velocity-porosity relationships in oceanic basalt from eastern flank of the Juan de Fuca Ridge: The effect of crack closure on seismic velocity, *Exploration Geophysics*, *39*, 4151.

Walsh, J. (1969), New analysis of attenuation in partially melted rock, *J. Geophys. Res.*, *74*(17), 4333–4337.

Wang, Z., and A. M. Nur (1989), Effects of CO_2 flooding on wave velocities in rocks with hydrocarbons, *SPE Reservoir Engineering*, *4*, 429–436.

Wang, Z., M. E. Cates, and R. T. Langan (1998), Seismic monitoring of a CO_2 flood in a carbonate reservoir: A rock physics study, *Geophysics*, *63*(5), 1604–1617, doi:10.1190/1.1444457.

Wilkens, R. H., G. J. Fryer, and J. Karsten (1991), Evolution of porosity and seismic structure of upper oceanic crust: Importance of aspect ratios, *J. Geophys. Res.*, *96*(B11), 17,981–17,995.

Xue, Z., and T. Ohsumi (2004), Seismic wave monitoring of CO_2 migration in water-saturated porous sandstone, *Exploration Geophysics*, *35*(1), 25–32.

Yam, H., and D. Schmitt (2011), Co2 rock physics: A laboratory study, *Canadian Well Logging Society Insite Magazine*, *30*, 13–16.